Site-specific modification of Alzheimer's peptides by cholesterol oxidation products enhances aggregation energetics and neurotoxicity

Kenji Usui[1,2], John D. Hulleman[1], Johan F. Paulsson[1], Sarah J. Siegel[1], Evan T. Powers[1], and Jeffery W. Kelly[3]

Departments of Chemistry and Molecular and Experimental Medicine, Scripps Research Institute and Skaggs Institute for Chemical Biology, 10550 North Torrey Pines Road, BCC265, La Jolla, CA 92037

Accumulation of amyloid β-peptide (Aβ) and tau aggregates, possibly linked to age-associated deficiencies in protein homeostasis, appear to cause Alzheimer's disease. Schiff-base formation between Aβ and the aldehyde-bearing cholesterol oxidation product 3-β-hydroxy-5-oxo-5,6-*seco*cholestan-6-al is known to increase Aβ amyloidogenicity. Here, we synthesized Aβ variants site-specifically modified with the cholesterol aldehyde at Asp-1, Lys-16, or Lys-28, rather than studying mixtures. These distinct modifications have a similar effect on the thermodynamic propensity for aggregation, enabling aggregation at low concentrations. In contrast, the modification site differentially influences the aggregation kinetics; Lys-16-modified Aβ formed amorphous aggregates fastest and at the lowest concentration (within 2 h at a concentration of 20 nM), followed by the Lys-28 and Asp-1 conjugates. Also, the aggregates resulting from Aβ Lys-16 cholesterol aldehyde conjugation were more toxic to primary rat cortical neurons than treatment with unmodified Aβ under identical conditions and at the same concentration. Our results show that Aβ modification by cholesterol derivatives, especially at Lys-16, renders it kinetically and thermodynamically competent to form neurotoxic aggregates at concentrations approaching the physiologic concentration of Aβ.

Aβ | amyloid | oxidative stress | oxidized metabolite | protein misfolding

Aging, associated with decreasing protein homeostasis (proteostasis) capacity and increasing oxidative stress, is a prominent amyloid disease risk factor (1, 2). The hallmark of these maladies is tissue-selective deposition of amorphous and/or fibrillar cross-β-sheet-rich protein assemblies called amyloid (3). Alzheimer's disease (AD) (4) is the most common amyloid disease, afflicting >5 million people over age 65 in the United States (5). AD appears to be exacerbated by, if not caused by, defects in proteostasis that lead to intra (6) and extracellular amyloid β-peptide amyloidogenesis (Aβ; 39–43-residue peptides produced by endoproteolytic processing of the amyloid precursor protein) (4), and to intracellular aggregation of tau (7). The 40-residue form of Aβ (Aβ_{40}) is most prevalent (8), whereas longer variants, especially the 42-residue form (Aβ_{42}), are the most amyloidogenic (9). The longer variants dominate Aβ deposits in the brains of patients with AD (10) and their levels are elevated in some familial forms of AD (11).

An important concept in the thermodynamics of amyloidogenesis is the critical concentration, the concentration below which amyloid cannot form (12). The Aβ_{40} critical concentration has been reported to be in the range of 1–30 μM (9, 13, 14). However, the physiologic concentration of Aβ_{40} in CSF is in the low nanomolar range (8). As mentioned above, Aβ_{42} is more amyloidogenic than Aβ_{40}, but its concentration is $\approx$10-fold lower than that of Aβ_{40} (8), so its critical concentration is still >100-fold higher than its physiologic concentration. How Aβ_{40} and Aβ_{42} aggregate in vivo when their physiologic concentrations are lower than their critical concentrations is one of the many mysteries of AD.

A related issue involves the kinetics of amyloid formation. Aβ is thought to undergo amyloidogenesis by a nucleated polymerization mechanism, which has two phases: a lag phase involving nucleation, followed by a fibril growth phase (12). The duration of the lag phase increases exponentially as concentration decreases, becoming very long when the concentration is close to the critical concentration (12). Thus, Aβ amyloidogenesis has both thermodynamic and kinetic barriers in vivo.

We have proposed that reversible covalent modification of Aβ by small molecule oxidation products, in combination with factors like adsorption to the extracellular matrix or membranes (15), can explain the ability of Aβ to form amyloid at physiologic concentrations (16–18). Small molecule oxidation products are generated when reactive oxygen species react with double bonds, including those of hydrophobic membrane components (19). The concentrations of the resulting hydrophobic aldehydes that can modify proteins through reversible Schiff base formation increase during aging and peak during oxidative stress (20). Both aging and oxidative stress are risk factors for AD (4, 19); in fact, small molecule oxidation products are found at elevated levels in the brains of individuals with AD (16, 19, 21, 22).

We and others have found that the naturally occurring small molecule oxidation products 4-hydroxynonenal (23) and 3β-hydroxy-5-oxo-5,6 *seco*cholestan-6-al (see **1** in Fig. 1*A*), derived from cholesterol, and the aldol product of the latter (see **2** in Fig. 1*A*) (24), covalently modify Aβ and increase its amyloidogenicity (16–18, 25–27). Prior data indicated that cholesterol oxidation products **1** and **2**, denoted **1(2)** hereafter because they interconvert via an aldol/retro-aldol reaction (16, 18, 24), react with Aβ via Schiff base formation at the *N*-terminal α-amine of Asp-1 (D1) and the side-chain ε-amines of Lys-16 (K16) and Lys-28 (K28) (18). Compounds **1** and **2** have been detected by us (18, 28) and others (29) in ex vivo human and rat brain samples at combined concentrations of up to 400 pg/mg of wet brain ($\approx$1 μM concentration). Scheinost et al. (27) recently suggested that K16 is the "hot spot" for Aβ aggregation induced by **1(2)** modification. We previously reported that adduct formation between Aβ_{40} and **1(2)** decreased the aggregation critical concentration to <100 nM (the limit of detection of the method used) (18), changed the aggregation mechanism from a nucleated to a downhill polymerization (17), and resulted in the
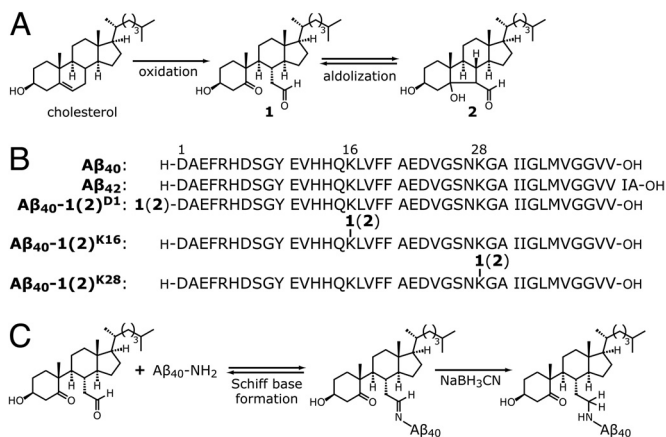
BIOPHYSICS AND COMPUTATIONAL BIOLOGY

Fig. 1. Oxidized cholesterol metabolites and their Aβ conjugates. (*A*) Cholesterol can be oxidized in vivo to form **1** and converted into **2** by a reversible aldol reaction. Compounds **1** and **2** can interconvert, so they are collectively denoted **1(2)**. (*B*) WT Aβ40 and Aβ42 sequences, and the sequences of the Aβ40-**1(2)** conjugates studied here. (*C*) Cholesterol metabolites **1(2)** can attach to an amine of Aβ (D1, K16, or K28) by Schiff base formation. Stable analogs were produced by reducing the Schiff bases with NaBH₃CN.

formation of spherical aggregates when incubated quiescently (17, 18), which are reported to be neurotoxic (30). Thus, a spike in the concentration of these hydrophobic aldehydes (e.g., caused by trauma or inflammation) could trigger Aβ aggregation and then become traceless if the aldehyde concentrations later decrease because of the reversibility of Schiff base formation. However, significant questions about the modification of Aβ by **1(2)** persist, including: Why is K16 a hot spot for covalent-modification-induced Aβ aggregation? Does modification by **1(2)** lower the critical concentration of Aβ aggregation into the physiologic concentration range? Can Aβ modified by **1(2)** aggregate at low concentrations on a biologically relevant time scale? And, are the aggregates formed by Aβ-**1(2)** conjugates toxic to primary neurons and what is their toxicity relative to unmodified Aβ? We address these questions here.

Results

Synthesis of Aβ Peptides Site-Specifically Modified by 1(2). To investigate the aggregation energetics of Aβ40 modified by **1(2)** at specific sites, we chemically synthesized Aβ40 modified with **1(2)** at the α-amine of D1 [Aβ40-**1(2)**^D1], or the ε-amine of K16 [Aβ40-**1(2)**^K16] or K28 [Aβ40-**1(2)**^K28] (Fig. 1*B*) using solid phase peptide synthesis (for detailed procedures, see *SI Materials and Methods*). Note that the hydrolytically unstable Schiff-base linkage between **1(2)** and Aβ was reduced to a secondary amine in each peptide-**1(2)** conjugate (Fig. 1*C*). Although this permanent covalent linkage through a secondary amine is less conformationally constrained than a Schiff base, it retains the positive charge at neutral pH and the ability to adopt a Schiff base-equivalent conformation of the hydrophobic appendage enabling aggregation at low concentrations.

Monomerization of Aβ40, Aβ42, and the Aβ40-1(2) Conjugates. Before studying the amyloidogenesis of Aβ40-**1(2)** conjugates, they must be monomerized. Because the Aβ40-**1(2)** conjugates are extremely aggregation prone, the high-pH pretreatment method of Fezoui et al. (31) that we used previously to monomerize Aβ40 (17, 18, 23) was not effective (Fig. S1). Instead, we monomerized the Aβ40-**1(2)** conjugates by dissolving them in 8 M guanidine hydrochloride (GuHCl) in phosphate buffer [50 mM sodium phosphate (NaPi), pH 7.5]. Solutions of monomeric Aβ variants in 8 M GuHCl were prepared for use by one of three methods.

(*i*) Solutions of Aβ variants for equilibrium aggregation experiments were simply filtered through a 0.2-μm filter and diluted to the desired peptide and GuHCl concentrations. (*ii*) Solutions of Aβ variants for kinetic experiments, requiring rigorously monomeric Aβ, were obtained by preparative size exclusion chromatography (SEC) using 8 M GuHCl as the mobile phase. (*iii*) GuHCl-free solutions of Aβ variants were prepared by passing the GuHCl solution through a short SEC column eluted with phosphate buffer (for further details, see *SI Materials and Methods*).

Critical Concentrations of the Aβ40-1(2) Conjugates. The critical concentration for aggregation, c_{agg}, is equivalent to the concentration of the monomeric protein left in solution when aggregation reaches equilibrium (12, 32). In principle, c_{agg} can be determined by allowing aggregation to reach equilibrium and measuring the concentration of Aβ40 monomer remaining in solution (32). However, the c_{agg} values of Aβ40-**1(2)** conjugates are well below the detection thresholds of most protein concentration determinations (18), so direct measurements are challenging, if not impossible.

Instead, we used a chaotrope denaturation strategy to estimate the c_{agg} values of Aβ40-**1(2)** conjugates. As suggested by Narimoto et al. (33), the free energy of aggregation, ΔG_{agg}, like the free energy of protein folding, should depend linearly on GuHCl concentration, as should the natural logarithm of c_{agg}, because $\Delta G_{agg} = -RT \ln c_{agg}$ (R is the gas constant and T is the temperature). Thus, c_{agg} should depend on GuHCl concentration as follows:

$$\ln c_{agg} = \ln c_{agg,0} + \frac{m_{agg}}{RT}[\text{GuHCi}] \qquad [1]$$

where [GuHCl] is the concentration of GuHCl, $c_{agg,0}$ is the critical concentration at 0 M GuHCl, and m_{agg}/RT is the slope of a plot of $\ln c_{agg}$ vs. [GuHCl]. According to Eq. **1**, $c_{agg,0}$ can be determined by measuring c_{agg} at a series of GuHCl concentrations, plotting $\ln c_{agg}$ vs. [GuHCl], and extrapolating to 0 M GuHCl.

The aggregate denaturation method described above was implemented as follows. Aβ40, Aβ42, and the Aβ40-**1(2)** conjugates were monomerized by method *i*. Solutions of each variant were diluted to make a set of solutions with increasing GuHCl concentrations but constant Aβ concentration. These sets of solutions were incubated at 37 °C under constant agitation for at least 5 days, after which they were filtered through a 0.2-μm filter, and the value of c_{agg} was determined by measuring the monomer concentration using the integrated peak intensities in a size exclusion chromatogram. To ensure that denaturation was reversible, preformed aggregates were also placed in increasing concentrations of GuHCl and c_{agg} was determined. The aggregates in question were fibrillar for Aβ40 and Aβ42 and amorphous for the Aβ40-**1(2)** conjugates. The c_{agg} values determined by approaching the aggregate-monomer equilibrium from the monomer or aggregate direction are plotted together vs. [GuHCl] for the Aβ variants in Fig. 2*A*. As expected for a true equilibrium, the c_{agg} values from the two methods are consistent and are fit to a single line. Fig. 2*B* (left axis, solid blue circles) shows the $c_{agg,0}$ values extrapolated from Fig. 2*A*. The critical concentration of Aβ40 determined by this method (850 nM) is similar to that determined previously by O'Nuallain et al. (14). The critical concentration of Aβ42 determined by this method is 160 nM, substantially lower than that of Aβ40, as expected (9).

The critical concentrations of Aβ40-**1(2)**^D1, Aβ40-**1(2)**^K16, and Aβ40-**1(2)**^K28 determined by the denaturation method (Fig. 2*B*) are the same within experimental error, averaging ≈4 nM. This value of c_{agg} is >200-fold lower than that of Aβ40 and 40-fold lower than that of Aβ42. The effect of the modification of Aβ40
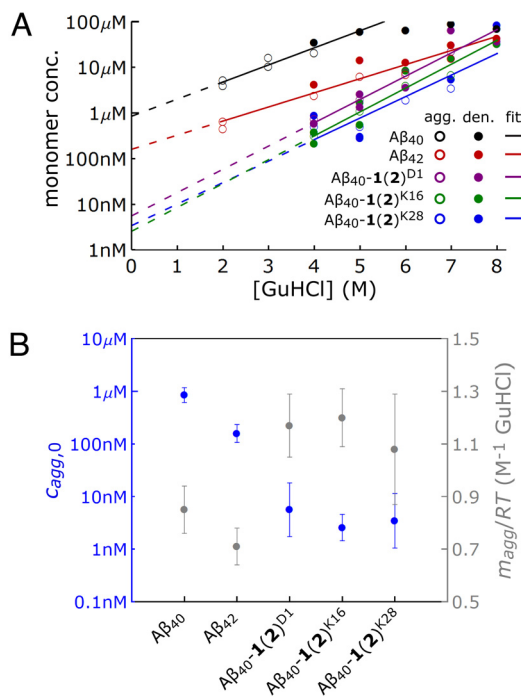
Fig. 2. Determination of $c_{agg,0}$ for Aβ variants. (*A*) Plots of Aβ_{40} (black), Aβ_{42} (red), Aβ_{40}-**1**(**2**)^{D1} (purple), Aβ_{40}-**1**(**2**)^{K16} (green), and Aβ_{40}-**1**(**2**)^{K28} (blue) monomer concentration vs. GuHCl concentration, [GuHCl]. Data points from aggregating Aβ variants at a given [GuHCl] (open circles). Data points from denaturing preformed aggregates at a given [GuHCl] (filled circles). Fits of Eq. **1** to the data (lines). Only data points between 2 and 5 M GuHCl were used in the fit for Aβ_{40}, because its c_{agg} is greater than the total peptide concentration when [GuHCl] > 5 M. Extrapolations of the fits to 0 M GuHCl for determining $c_{agg,0}$ (dashed lines). (*B*) Blue axis: estimates for the aggregation critical concentrations ($c_{agg,0}$) at 0 M GuHCl of the Aβ variants (*Left*). Gray axis: slopes (m_{agg}/RT) of the fits of Eq. **1** to the data in *A* (*Right*). Error bars are SEM.

by **1**(**2**) on Aβ_{40} aggregation thermodynamics is apparently strong enough to drive $c_{agg,0}$ of the Aβ_{40}-**1**(**2**) conjugates into the physiologic concentration range of Aβ, and is independent of the site of modification.

The slopes of the plots of ln c_{agg} vs. [GuHCl] in Fig. 2*A* for the Aβ variants are also plotted in Fig. 2*B* (right axis, solid gray circles). The Aβ_{40}-**1**(**2**) conjugates have slopes $\approx$1.2 M^{-1} GuHCl (corresponding to $m_{agg} = 0.7$ kcal mol^{-1} M^{-1} GuHCl), compared with 0.85 M^{-1} GuHCl ($m_{agg} = 0.52$ mol^{-1} M^{-1} GuHCl) and 0.71 M^{-1} GuHCl ($m_{agg} = 0.44$ kcal mol^{-1} M^{-1} GuHCl) for unmodified Aβ_{40} and Aβ_{42}, respectively. The value of m_{agg} should be proportional to the accessible surface area buried during aggregation (34). Assuming that m_{agg} increases by 2.2 $\times$ 10^{-4} kcal mol^{-1} M^{-1} GuHCl per Å^2 of buried surface area (34), the difference in m_{agg} values suggests that the Aβ_{40}-**1**(**2**) conjugates bury $\approx$900 Å^2 more surface area on aggregation than unmodified Aβ_{40}, comparable with the accessible surface area of cholesterol ($\approx$670 Å^2).

Aggregation Kinetics of Aβ_{40}-1(2) Conjugates Monitored by Light Scattering. Samples for studying the aggregation rates of the Aβ_{40}-**1**(**2**) conjugates were monomerized by method *ii*, yielding rigorously monomeric Aβ_{40}-**1**(**2**). The fractions corresponding to monomeric Aβ_{40}-**1**(**2**) were collected, diluted so that the GuHCl concentration was 0.8 M, and the peptide concentration was as desired, and aggregation was monitored (without agitation) by the intensity of the light scattered at 90°, ΔI_s (90°).

The aggregation time courses of Aβ_{40}, Aβ_{42}, and the Aβ_{40}-**1**(**2**) conjugates at 37 °C in phosphate buffer (50 mM NaPi/300 mM
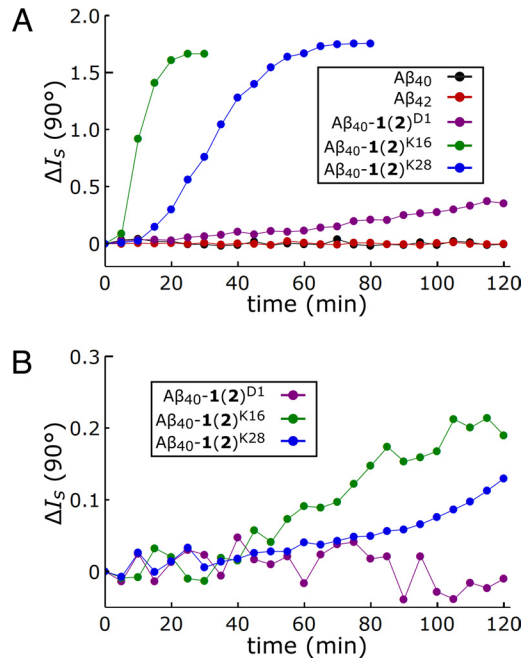

Fig. 3. Aggregation kinetics of Aβ variants at low concentrations monitored by light scattering. (*A*) Representative light scattering intensity changes, ΔI_s (90°), vs. time for Aβ_{40} (black), Aβ_{42} (red), Aβ_{40}-**1**(**2**)^{D1} (purple), Aβ_{40}-**1**(**2**)^{K16} (green), and Aβ_{40}-**1**(**2**)^{K28} (blue) at concentrations of 500 nM. (*B*) Representative ΔI_s (90°) vs. time for Aβ_{40}-**1**(**2**)^{D1} (purple), Aβ_{40}-**1**(**2**)^{K16} (green), and Aβ_{40}-**1**(**2**)^{K28} (blue) at concentrations of 100 nM. Analogous data using concentrations <100 nM are shown in Fig. S2.

NaCl, pH 7.5) with 0.8 M GuHCl present are plotted in Fig. 3*A* (500 nM) and 3*B* (100 nM). Unmodified Aβ_{40} and Aβ_{42} did not aggregate on the time scale of these experiments (2 h) at concentrations of 500 nM. In contrast, the Aβ_{40}-**1**(**2**) conjugates showed evidence of aggregation within 2 h at a concentration of 500 nM (Fig. 3*A*). Unlike aggregation thermodynamics, the aggregation rates of the Aβ_{40}-**1**(**2**) conjugates depended strongly on the modification site. Aβ_{40}-**1**(**2**)^{K16} aggregated faster than Aβ_{40}-**1**(**2**)^{K28}, which aggregated faster than Aβ_{40}-**1**(**2**)^{D1}. This ordering is maintained at concentrations of 100 nM, except that Aβ_{40}-**1**(**2**)^{D1} no longer aggregated within 2 h (Fig. 3*B*). Although the light scattering data were noisy at even lower Aβ_{40}-**1**(**2**) concentrations, Aβ_{40}-**1**(**2**)^{K16} and Aβ_{40}-**1**(**2**)^{K28} still aggregated at concentrations of 50 nM, the limit of detection (aggregation reactions at 20 nM were examined, but exhibited no signal above the background; see Fig. S2).

Immuno-Electron Microscopy of Samples from Low Concentration Light Scattering Experiments. Samples from the low concentration light scattering time courses were examined by immuno-EM to ensure that the aggregates detected were composed of Aβ_{40}-**1**(**2**), and to attempt to detect aggregates at even lower concentrations. Aliquots (50 μL) were removed from the aggregation reactions after 2 h and applied to EM grids. These EM grids were incubated with a monoclonal anti-Aβ antibody (6E10) followed by protein A (which binds to 6E10) conjugated to 10-nm gold particles. The resulting EM images are shown in Fig. 4 and Fig. S3 (for experimental details, see *SI Materials and Methods*). No aggregates were observed in samples of Aβ_{40} after 2 h of aggregation at a concentration of 500 nM (Fig. 4*A*), but gold particles were readily visible covering samples of Aβ_{40} fibrils formed at 25 μM (Fig. 4*B*). Aβ_{42} also showed no evidence of aggregation at 500 nM after 2 h (Fig. 4*C*), despite this concentration being above its apparent critical concentration. The
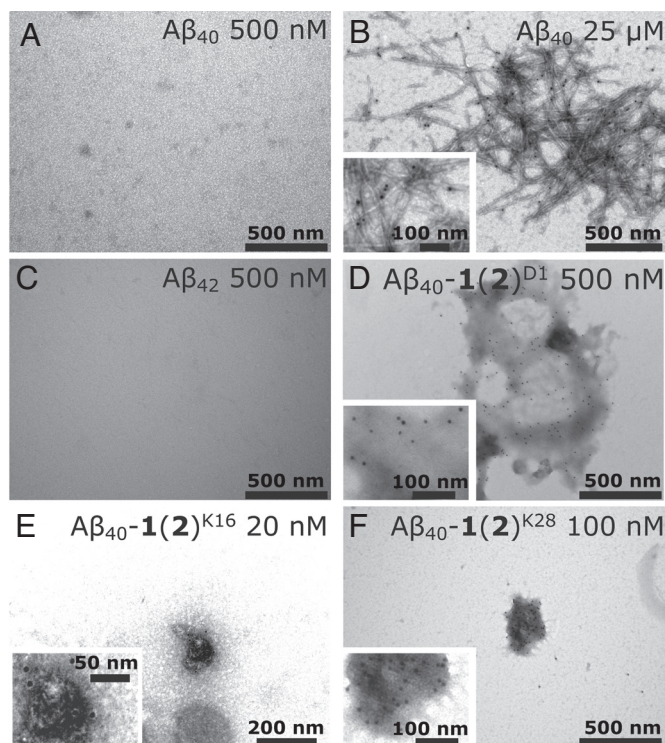
Fig. 4. Immuno-EM images of aggregates formed (or not formed) by $A\beta$ variants. (*A*) Representative image from a sample in which $A\beta_{40}$ at a concentration of 500 nM was incubated at 37 °C for 2 h. No $A\beta$ aggregates were observed. (*B*) Representative image of preformed unmodified $A\beta_{40}$ fibrils formed in a solution of $A\beta_{40}$ (25 μM) at 37 °C with agitation. Gold particles (black dots), indicating the presence of $A\beta_{40}$, can be seen attached to fibrils. (*C*) As in *A*, but with $A\beta_{42}$. (*D*) As in *A*, but with $A\beta_{40}$-**1**(**2**)^{D1} at a concentration of 500 nM. (*E*) As in *A*, but with $A\beta_{40}$-**1**(**2**)^{K16} at a concentration of 20 nM. (*F*) As in *A*, but with $A\beta_{40}$-**1**(**2**)^{K28} at a concentration of 100 nM. Aggregates of $A\beta_{40}$-**1**(**2**) conjugates were not detected by this method in samples at concentrations lower than those noted in *D–F*. Additional immuno-EM images are shown in Fig. S3.

remaining panels of Fig. 4 show images from the lowest concentration samples in which aggregates could be found in the 2-h aggregation reactions of the $A\beta_{40}$-**1**(**2**) conjugates. Amorphous aggregates were detected at 500 nM for $A\beta_{40}$-**1**(**2**)^{D1} (Fig. 4*D*), at 20 nM for $A\beta_{40}$-**1**(**2**)^{K16} (Fig. 4*E*), and at 100 nM for $A\beta_{40}$-**1**(**2**)^{K28} (Fig. 4*F*). Given that these are the minimal concentrations at which aggregates could be detected, the aggregates shown in Fig. 4 *D–F* were infrequently detected on the EM grids, as expected. Utilization of an $A\beta$-specific antibody guarantees that the aggregates are composed of $A\beta$. Also, the fact that aggregates are not observed in the unmodified $A\beta$ samples suggests that they are not spurious. These results extend the light scattering data described above by demonstrating that $A\beta_{40}$-**1**(**2**)^{K16} aggregates at concentrations below the light scattering detection limit.

Aggregation Kinetics of the $A\beta_{40}$-1(2) Conjugates Monitored by Thioflavin T (TfT) Fluorescence. $A\beta_{40}$, $A\beta_{42}$, and the $A\beta_{40}$-**1**(**2**) conjugates were monomerized by method *iii* and diluted to a concentration of 10 μM in phosphate buffer (50 mM NaPi/300 mM NaCl, pH 7.5). Their TfT-monitored aggregation time courses are shown in Fig. S4. Aggregates that yield a TfT fluorescence signal do not necessarily have classic fibrillar morphologies (17, 18, 35, 36), and therefore, will be termed "microfibrillar." These experiments were performed with mild agitation (5 s of shaking every 10 min) to encourage the transition to microfibrillar
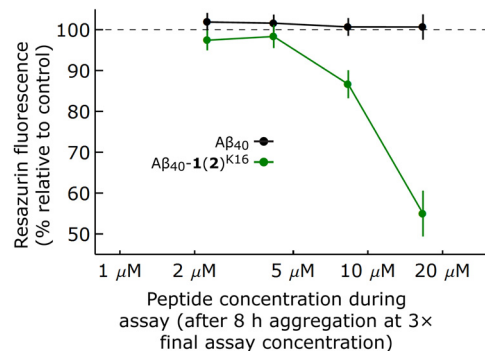

Fig. 5. Neurotoxicity of $A\beta_{40}$ vs. $A\beta_{40}$-**1**(**2**)^{K16}. $A\beta_{40}$ (black) and $A\beta_{40}$-**1**(**2**)^{K16} (green) were subjected to aggregation conditions quiescently for 8 h (6.75 μM to 50 μM, 3× the final concentration used in the toxicity assay) and applied to primary rat cortical neurons at final concentrations ranging from 0 to 16.67 μM. After 48 h of incubation, the viability of the cells was assessed by resazurin fluorescence. Viability is shown as a percentage of the metabolic activity of cells treated with buffer alone. Data are from independent triplicates, and the error bars are for SEM. Fig. S6, which reveals neuron atrophy and disruption of neural connections only in $A\beta_{40}$-**1**(**2**)^{K16}-treated neurons, further supports the toxicity of $A\beta_{40}$-**1**(**2**)^{K16}, but not $A\beta_{40}$ under these aggregation conditions.

aggregates (17). Microfibrillar aggregates appeared fastest for $A\beta_{40}$-**1**(**2**)^{D1}, followed by $A\beta_{40}$-**1**(**2**)^{K16} and then $A\beta_{40}$-**1**(**2**)^{K28}, although more slowly in every case than the aggregates detected in the light scattering experiments, despite higher concentrations being used. This result suggests that the amorphous aggregates detected by light scattering are TfT-negative (i.e., they are not microfibrillar), and the amorphous aggregates either form first and then convert to microfibrillar aggregates or the amorphous and microfibrillar aggregates form in parallel with the amorphous aggregates appearing somewhat faster. We prefer the first explanation, because the second implies that the TfT-negative amorphous aggregates are off-pathway. The TfT-monitored time courses are not consistent with amyloidogenesis with off-pathway aggregates, because the TfT fluorescence does not increase quadratically with time, as required by off-pathway aggregation (37). Also, we have shown previously that amorphous aggregates formed by $A\beta_{40}$-**1**(**2**) conjugates can convert directly to fibrils on seeding or agitation (17, 18).

Toxicity of the Aggregates Formed by $A\beta_{40}$-1(2)^{K16} to Primary Neurons. Although modification of $A\beta_{40}$ with **1**(**2**) dramatically lowers $c_{agg,0}$ and hastens aggregate formation, whether these aggregates are toxic to primary neurons is unknown. The neurotoxicities of $A\beta_{40}$ and $A\beta_{40}$-**1**(**2**)^{K16} were compared by first monomerizing each variant by method *iii*, except that the peptides were eluted from the gel filtration column with HBSS. $A\beta_{40}$ and $A\beta_{40}$-**1**(**2**)^{K16} were incubated in HBSS for 8 h at 6.75 to 50 μM (3× the final toxicity assay concentration) at room temperature under quiescent conditions. After the incubation period, glial-cell-free primary rat cortical neurons (Fig. S5) were incubated for 48 h with varying concentrations of the $A\beta$ peptides (0- to 16.67-μM final concentration) in cell culture media. The solutions of unmodified $A\beta_{40}$ had little effect on cell viability/metabolic activity relative to buffer control at all concentrations under these aggregation conditions (Fig. 5), as determined by a resazurin assay (38). This result is consistent with our previous observation that rigorously monomerized, unmodified $A\beta_{40}$ does not aggregate within 8 h when it is not agitated (17, 18). In contrast, the solutions of $A\beta_{40}$-**1**(**2**)^{K16} were toxic to cells at concentrations >4.17 μM (up to a 45 ± 4% reduction in cell viability at 16.67 μM relative to buffer-treated controls; Fig. 5). The deleterious effect of $A\beta_{40}$-**1**(**2**)^{K16} aggregates on the neurons are also apparent from the altered cell morphologies. Phase

contrast microscopy images of primary rat cortical neurons incubated for 48 h with HBSS or Aβ_{40} at a final concentration of 16.67 μM revealed healthy neurons that formed interconnected networks (Fig. S6 *A* and *B*). However, primary rat cortical neurons incubated for 48 h with Aβ_{40}-**1(2)**^{K16} at an identical concentration exhibited atrophy, clumping, and a loss of neural connections (Fig. S6*C*). These results demonstrate that the Aβ_{40}-**1(2)** conjugate at K16 forms neurotoxic aggregates under conditions where Aβ_{40} does not.

Discussion

We have shown that the Aβ_{40}-**1(2)** conjugates are thermodynamically and kinetically competent to form amorphous aggregates in vitro at concentrations close to the physiologic concentration of Aβ. However, their kinetic competence, unlike their thermodynamic competence, depends strongly on the site of modification. Aβ_{40}-**1(2)**^{K16} forms aggregates most rapidly and at the lowest concentration (within 2 h at a concentration of 20 nM), followed by Aβ_{40}-**1(2)**^{K28} and Aβ_{40}-**1(2)**^{D1}. This ranking matches the local hydrophobicity of the Aβ sequence at the modification site: K16 resides in the most hydrophobic context (…VHHQ*K*LVFF…), followed by K28 (…VGSN*K*GAII…), and then D1 (*D*AEFRHDSG…). This correlation between local hydrophobicity and the kinetic effect of metabolite modification suggests that K16 and its surrounding residues were already important for aggregate nucleation and growth, consistent with previous findings (39), and that the increase in hydrophobicity attendant to the attachment of **1(2)** to K16 magnifies the influence of this region. Thus, it is a hotspot for hydrophobic metabolite modification-mediated aggregation.

Fig. S4 shows that the formation of microfibrillar species is fastest for Aβ_{40}-**1(2)**^{D1}, followed by Aβ_{40}-**1(2)**^{K16}, and then by Aβ_{40}-**1(2)**^{K28}. This ranking matches the proximity of the modification to the *N* terminus rather than correlating with local hydrophobicity. We posit that the microfibrillar species result from conformational rearrangements within the initially-formed amorphous aggregates, consistent with the expectation that the transition from the TfT-negative amorphous aggregates to microfibrillar aggregates requires larger conformational changes at K28 and K16 than at D1, which is known to be disordered in structural models of fibrillar Aβ (40, 41).

Our observation that Aβ_{40}-**1(2)**^{D1} and Aβ_{40}-**1(2)**^{K28} are highly aggregation prone appear to contradict the results of Scheinost et al. (27), who reported that Aβ_{40} variants in which Schiff base formation was blocked at the ε-amine of K16 did not form TfT-positive aggregates in the presence of **1(2)**, even when the α-amine of D1 and the ε-amine of K28 were available. Our results can be reconciled with those of Scheinost et al. (27) by noting that Schiff base formation is reversible and Schiff bases are unstable in aqueous solution. Therefore, the concentration of Aβ_{40}-**1(2)** conjugates should be low when Aβ_{40} is mixed with exogenous **1(2)**. Our results show that Aβ_{40}-**1(2)**^{K16}, which aggregates most rapidly at the lowest concentration, should be best able to aggregate under such conditions.

It is likely that no single factor will fully explain the pathogenesis of AD. AD probably results from the balance between Aβ aggregation and aggregate clearance tipping toward the former on aging, leading to aggregate accumulation, neurotoxicity, and memory loss. It is probable that the sum of all of the factors that either promote aggregation or diminish aggregate clearance determine whether an individual will become afflicted with AD. We have shown that Aβ modification by the oxidized

cholesterol metabolite **1(2)**, especially at K16, could be an especially potent promoter of Aβ aggregation. Aβ_{40}-**1(2)**^{K16} is, to our knowledge, the only Aβ variant that is kinetically and thermodynamically competent to aggregate at concentrations approaching the physiologic concentration of Aβ. Also, we have demonstrated that the aggregates formed by Aβ_{40}-**1(2)**^{K16} are toxic to primary neurons. These observations, especially when considered with the previous demonstration that Aβ_{40}-**1(2)** conjugates can induce unmodified Aβ to coaggregate (18), suggest that metabolite-initiated amyloid formation could contribute to AD pathogenesis. These data also imply that inhibiting Aβ modification by oxidized metabolites by using aldehyde-sequestering compounds or the equivalent could be a viable preventative strategy against AD (16, 17, 42). However, future efforts will be required to better understand the role of membrane component-derived Schiff base modifications of Aβ in the etiology of AD.

Methods

For detailed descriptions of the synthesis of Aβ variants site-specifically modified with **1(2)** and the procedures for monomerization, immuno-EM, TfT-monitored aggregation kinetics, and the primary rat cortical neuron-based toxicity assay, see SI Materials and Methods. The solvent accessible surface area of cholesterol was determined by using ChemBio3D Ultra (probe radius = 1.4 Å).

Estimating Critical Concentrations Using GuHCl Denaturation and SEC. Solutions of Aβ_{40}, Aβ_{42}, Aβ_{40}-**1(2)**^{D1}, Aβ_{40}-**1(2)**^{K16}, and Aβ_{40}-**1(2)**^{K28} monomerized by method *i* (see SI Materials and Methods) were diluted to a peptide concentration of 100 μM and GuHCl concentrations ranging from 2 to 8 M in 1 M increments. These solutions were incubated with agitation using an Echo-Therm RT10 rotating mixer (Torrey Pines Scientific) at 20 rpm for >5 days at 37 °C to enable aggregation. Alternately, preformed aggregates of each Aβ variant were prepared by monomerizing the peptides by method *i*, diluting to a peptide concentration of 100 μM and a GuHCl concentration of 0.8 M, and incubating at 37 °C with agitation as above for >5 days. Preformed aggregates were also prepared by directly dissolving the Aβ variants in buffer and incubating at 37 °C with agitation. Solutions of preformed aggregates, prepared with or without monomerization, were diluted to final peptide concentrations of 10 or 100 μM, respectively, and final GuHCl concentrations between 2 and 8 M to denature aggregates, and then incubated with agitation (20 rpm, 37 °C, >5 days).

Aggregation and aggregate denaturation solutions were filtered through a 0.22-μm syringe filter (Millipore). Samples (100 μL) were injected onto an AKTA FPLC employing a Superdex 75 HR 10/30 SEC column (GE Healthcare) and eluted with 50 mM sodium phosphate (pH 7.5, 0.02% NaN$_3$) containing GuHCl at the same concentration as the injected sample. Aβ variants were detected by absorbance at 280 nm. Concentrations of monomeric Aβ variants were determined from the integrated intensity of the monomer peaks.

Kinetics of Aggregation of Aβ Variants Monitored by Light Scattering. Seed-free solutions of Aβ_{40}, Aβ_{42}, and Aβ-**1(2)** conjugates in 8 M GuHCl prepared by method *ii* (see SI Materials and Methods) were diluted with 8 M GuHCl to 10× the desired final peptide concentration. These solutions were then diluted 10-fold in phosphate buffer (50 mM NaPi/300 mM NaCl, pH 7.5) so that the GuHCl concentration was 0.8 M and the peptide concentration was as desired. Samples (5 mL) were transferred to 25 mL scintillation vials, which were placed in a Dawn EOS light scattering photometer (Wyatt Technology) with a Peltier temperature controller. Light scattering intensity data at 90° offset by the intensity at t = 0 min, or ΔI_s (90°), were collected for 2 h at 37 °C.

1. Balch WE, Morimoto RI, Dillin A, Kelly JW (2008) Adapting proteostasis for disease intervention. *Science* 319:916–919.
2. Cohen E, Bieschke J, Perciavalle RM, Kelly JW, Dillin A (2006) Opposing activities protect against age-onset proteotoxicity. *Science* 313:1604–1610.
3. Kelly JW (1996) Alternative conformations of amyloidogenic proteins govern their behavior. *Curr Opin Struct Biol* 6:11–17.
4. Tanzi RE, Bertram L (2005) Twenty years of the Alzheimer's disease amyloid hypothesis: A genetic perspective. *Cell* 120:545–555.

5. Hebert LE, Scherr PA, Bienias JL, Bennett DA, Evans DA (2003) Alzheimer disease in the US population: Prevalence estimates using the 2000 census. *Arch Neurol* 60:1119–1122.
6. LaFerla FM, Green KN, Oddo S (2007) Intracellular amyloid-β in Alzheimer's disease. *Nat Rev Neurosci* 8:499–509.
7. Ballatore C, Lee VM, Trojanowski JQ (2007) Tau-mediated neurodegeneration in Alzheimer's disease and related disorders. *Nat Rev Neurosci* 8:663–672.
8. Mehta PD, Pirttila T, Patrick BA, Barshatzky M, Mehta SP (2001) Amyloid β protein 1–40 and 1–42 levels in matched cerebrospinal fluid and plasma from patients with Alzheimer disease. *Neurosci Lett* 304:102–106.
9. Jarrett JT, Berger EP, Lansbury PT, Jr (1993) The carboxy terminus of the β-amyloid protein is critical for the seeding of amyloid formation: Implications for the pathogenesis of Alzheimer's disease. *Biochemistry* 32:4693–4697.
10. Iwatsubo T, et al. (1994) Visualization of Aβ 42(43) and Aβ 40 in senile plaques with end-specific Aβ monoclonals: Evidence that an initially deposited species is Aβ 42(43). *Neuron* 13:45–53.
11. Suzuki N, et al. (1994) An increased percentage of long amyloid-β protein secreted by familial amyloid-β protein precursor (βAPP717) mutants. *Science* 264:1336–1340.
12. Powers ET, Powers DL (2006) The kinetics of nucleated polymerizations at high concentrations: Amyloid fibril formation near and above the ''supercritical concentration.'' *Biophys J* 91:122–132.
13. Hortschansky P, Christopeit T, Schroeckh V, Fandrich M (2005) Thermodynamic analysis of the aggregation propensity of oxidized Alzheimer's β-amyloid variants. *Protein Sci* 14:2915–2918.
14. O'Nuallain B, Shivaprasad S, Kheterpal I, Wetzel R (2005) Thermodynamics of Aβ(1–40) amyloid fibril elongation. *Biochemistry* 44:12709–12718.
15. Matsuzaki K (2007) Physicochemical interactions of amyloid beta-peptide with lipid bilayers. *Biochim Biophys Acta* 1768:1935–1942.
16. Bieschke J, et al. (2006) Small molecule oxidation products trigger disease-associated protein misfolding. *Acc Chem Res* 39:611–619.
17. Bieschke J, Zhang Q, Powers ET, Lerner RA, Kelly JW (2005) Oxidative metabolites accelerate Alzheimer's amyloidogenesis by a two-step mechanism, eliminating the requirement for nucleation. *Biochemistry* 44:4977–4983.
18. Zhang Q, et al. (2004) Metabolite-initiated protein misfolding may trigger Alzheimer's disease. *Proc Natl Acad Sci USA* 101:4752–4757.
19. Sayre LM, Smith MA, Perry G (2001) Chemistry and biochemistry of oxidative stress in neurodegenerative disease. *Curr Med Chem* 8:721–738.
20. Voss P, Siems W (2006) Clinical oxidation parameters of aging. *Free Radic Res* 40:1339–1349.
21. Markesbery WR, Lovell MA (1998) Four-hydroxynonenal, a product of lipid peroxidation, is increased in the brain in Alzheimer's disease. *Neurobiol Aging* 19:33–36.
22. Montine TJ, Markesbery WR, Morrow JD, Roberts LJ, II (1998) Cerebrospinal fluid F2-isoprostane levels are increased in Alzheimer's disease. *Ann Neurol* 44:410–413.
23. Siegel SJ, Bieschke J, Powers ET, Kelly JW (2007) The oxidative stress metabolite 4-hydroxynonenal promotes Alzheimer protofibril formation. *Biochemistry* 46:1503–1510.
24. Wentworth P, Jr, et al. (2003) Evidence for ozone formation in human atherosclerotic arteries. *Science* 302:1053–1056.
25. Komatsu H, Liu L, Murray IV, Axelsen PH (2007) A mechanistic link between oxidative stress and membrane mediated amyloidogenesis revealed by infrared spectroscopy. *Biochim Biophys Acta* 1768:1913–1922.
26. Murray IV, et al. (2007) Membrane-mediated amyloidogenesis and the promotion of oxidative lipid damage by amyloid-β proteins. *J Biol Chem* 282:9335–9345.
27. Scheinost JC, Wang H, Boldt GE, Offer J, Wentworth P, Jr (2008) Cholesterol secosterol-induced aggregation of methylated amyloid-β peptides-Insights into aldehyde-initiated fibrillization of amyloid-β. *Angew Chem Int Ed Engl* 47:3919–3922.
28. Bosco DA, et al. (2006) Elevated levels of oxidized cholesterol metabolites in Lewy body disease brains accelerate alpha-synuclein fibrilization. *Nat Chem Biol* 2:249–253.
29. Karu K, et al. (2007) Liquid chromatography-mass spectrometry utilizing multi-stage fragmentation for the identification of oxysterols. *J Lipid Res* 48:976–987.
30. Klein WL, Stine WB, Jr, Teplow DB (2004) Small assemblies of unmodified amyloid β-protein are the proximate neurotoxin in Alzheimer's disease. *Neurobiol Aging* 25:569–580.
31. Fezoui Y, et al. (2000) An improved method of preparing the amyloid β-protein for fibrillogenesis and neurotoxicity experiments. *Amyloid* 7:166–178.
32. O'Nuallain B, et al. (2006) Kinetics and thermodynamics of amyloid assembly using a high-performance liquid chromatography-based sedimentation assay. *Methods Enzymol* 413:34–74.
33. Narimoto T, et al. (2004) Conformational stability of amyloid fibrils of β2-microglobulin probed by guanidine-hydrochloride-induced unfolding. *FEBS Lett* 576:313–319.
34. Myers JK, Pace CN, Scholtz JM (1995) Denaturant m values and heat capacity changes: Relation to changes in accessible surface areas of protein unfolding. *Protein Sci* 4:2138–2148.
35. Frankenfield KN, Powers ET, Kelly JW (2005) Influence of the N-terminal domain on the aggregation properties of the prion protein. *Protein Sci* 14:2154–2166.
36. Hurshman AR, White JT, Powers ET, Kelly JW (2004) Transthyretin aggregation under partially denaturing conditions is a downhill polymerization. *Biochemistry* 43:7365–7381.
37. Powers ET, Powers DL (2008) Mechanisms of protein fibril formation: Nucleated polymerization with competing off-pathway aggregation. *Biophys J* 94:379–391.
38. O'Brien J, Wilson I, Orton T, Pognan F (2000) Investigation of the Alamar Blue (resazurin) fluorescent dye for the assessment of mammalian cell cytotoxicity. *Eur J Biochem* 267:5421–5426.
39. Hilbich C, Kisters-Woike B, Reed J, Masters CL, Beyreuther K (1992) Substitutions of hydrophobic amino acids reduce the amyloidogenicity of Alzheimer's disease βA4 peptides. *J Mol Biol* 228:460–473.
40. Luhrs T, et al. (2005) 3D structure of Alzheimer's amyloid-β(1–42) fibrils. *Proc Natl Acad Sci USA* 102:17342–17347.
41. Petkova AT, Yau WM, Tycko R (2006) Experimental constraints on quaternary structure in Alzheimer's β-amyloid fibrils. *Biochemistry* 45:498–512.
42. Negre-Salvayre A, Coatrieux C, Ingueneau C, Salvayre R (2008) Advanced lipid peroxidation end products in oxidative damage to proteins. Potential role in diseases and therapeutic prospects for the inhibitors. *Br J Pharmacol* 153:6–20.